On the role of aortic valve architecture for physiological haemodynamics and valve replacement. Part II: spectral analysis and anisotropy

Pascal Corso (pascal.corso@unibe.ch)
University of Bern https://orcid.org/0000-0001-7875-1080
Dominik Obrist
University of Bern

Research Article

Keywords: Aortic stentosis, Bioprosthetic aortic valve, Flow turbulence, Fluid-Structure Interaction simulations, Kinetic energy anisotropy, Spectral analysis, Valve design

Posted Date: September 27th, 2023

DOI: https://doi.org/10.21203/rs.3.rs-3387570/v1

On the role of aortic valve architecture for physiological haemodynamics and valve replacement. Part II: spectral analysis and anisotropy.

Pascal Corso[1], Dominik Obrist[1]

Affiliations: [1]ARTORG Center for Biomedical Engineering Research, University of Bern, Bern, Switzerland.

Correspondence: Pascal Corso, University of Bern, Bern, Switzerland.

E-mail: pascal.corso@unibe.ch

Abstract

Severe aortic valve stenosis can lead to heart failure and aortic valve replacement (AVR) is the primary treatment. However, increasing prevalence of aortic stenosis cases reveal limitations in current replacement options, necessitating improved prosthetic aortic valves. In this study, we investigate flow disturbances downstream of severe aortic stenosis and two bioprosthetic aortic valve (BioAV) designs using advanced energy-based analyses. Spectral analysis shows kinetic energy (KE) decay variations, with the stenotic case aligning with Kolmogorov's theory, while BioAVs differ. We explore the impact of flow helicity on KE transfer and decay in BioAVs. Probability distributions of modal KE anisotropy unveil flow asymmetries in the stenotic and one BioAV case. Moreover, an inverse correlation between modal KE anisotropy and normalised helicity intensity is noted, with the coefficient of determination varying among the valve configurations. Leaflet dynamics analysis highlights a stronger correlation between flow and biomechanical KE anisotropy in one BioAV due to higher leaflet displacement magnitude. These findings emphasise the role of valve architecture in aortic turbulence and its significance for BioAV performance and energy-based design optimisation.

Main

Calcific aortic valve stenosis is characterised by a progressive deterioration, remodelling and thickening of the native aortic valve leaflet tissue, causing a reduction in its functional flexibility. This condition, referred to as aortic stenosis (AS), results in increased resistance to blood flow from the left ventricle to the aorta, particularly during systole and the potential for blood regurgitation during diastole[6,7,29]. The long-term implications of this pathology are serious. The AS is indeed generally defined as severe when a significant left ventricular outflow tract (LVOT) obstruction leading to a reduced orifice area and high downstream jet velocity is present and symptoms such as dyspnea, heart failure, chest pain or syncope appear[3]. To address this critical issue, the replacement with valvular prostheses has emerged as a prevalent solution. These prostheses come in two primary types: mechanical heart valves made from rigid materials such as titanium or carbon and bioprosthetic or tissue aortic valves (BioAVs) manufactured based on biological tissue. The replacement of the diseased native aortic valve is achieved through a medical procedure known as aortic valve replacement (AVR). Aortic valve stenotic disease is the most commonly occurring valvular pathology in developed countries (afflicting 9 million people worldwide) and its prevalence has been increasing with population ageing[1]. Moreover, surgical aortic valve replacements tally around 300,000 cases annually and this number is projected to double by 2050 due to the ageing global population[21].

Previous studies have extensively explored the haemodynamic performance of aortic valves made from biological materials like porcine or bovine pericardium[2,4,6,13,27,29]. However, the correlation between the kinetic energy (KE) present within the valve components (i.e. leaflets and supporting ring) and the energy carried by the turbulent structures in the flow surrounding the BioAV has yet to be investigated, either *in vitro* or *in silico*.

In their work, Bescek *et al.*[4] presented a broad computational characterisation of the turbulent features of the flow downstream of one bioprosthetic aortic valve model under peak systolic conditions. One-dimensional wavenumber energy spectra were calculated at various distances from the sino-tubular junction and it was argued that the spectra based on points diametrically aligned where the turbulent dissipation rate is the largest could be connected to shear-induced thrombocyte activation. Finally, it was noticed the presence of zones with elevated and fluctuating wall shear stress at the aortic wall that could possibly underline the presence of endothelial lesions in these zones. Nonetheless, the wavenumber kinetic energy spectra considered in Becsek et al.[4] were one-dimensional and limited to a confined region of the flow along a line perpendicular to the centerline, thus excluding the study of anisotropy in the kinetic energy (KE).

Besides, in Corso *et al.*[6,7,8], similar conclusions were drawn using both *in vitro* three-dimensional particle tracking velocimetry experiments and from direct numerical simulation downstream of a stenotic aortic valve as to the detrimental effect of turbulence on blood platelet damage and on the production of important pressure loss due to elevated haemodynamic turbulent stresses. Moreover, it was emphasised that taking into account Reynolds' stress close to the wall for the accurate evaluation of the wall shear stress from flow field data with limited spatial resolution is crucial when disturbed aortic flows are considered.

Recently, Gallo *et al.* have explored the relationship between phase-averaged and fluctuating helicity and phase-averaged and turbulent kinetic energy for one model of mechanical heart valve prostheses and for one model of bioprosthetic valve. To this end, they simulated the coupled fluid-structure interaction problem by applying the interface conditions through an immersed body surface method. It was found in the study that haemodynamics downstream of the mechanical valve presenting larger phase-averaged and fluctuating helicity than that downstream of bioprosthetic valve. For both heart valve types, strong linear correlations were found between volume-averaged kinetic energy and helicity when considering phase-averaged or fluctuating quantities. Peaks of turbulent kinetic energy or fluctuating helicity for both heart valve types was delayed as compared to the peaks of mean kinetic energy and phase-averaged helicity. Despite this study introduces novelty regarding the relationship between flow helicity and kinetic energy and despite the use of 20 simulated cardiac cycles to compute flow field statistics, several limitations should be recognized. These include the use of a simplified mass-spring model to solve the dynamics of the deformable leaflets, the assumption of a rigid aortic wall and the absence of a ring supporting the valve leaflets in the simulations. Furthermore, an in-depth examination of the spatial distribution of kinetic energy, helicity, and their relationship to leaflet and valve designs was not established.

The present work is the second part of a comprehensive two-part study. Both parts utilise validated and high-fidelity computational approaches. In this paper, the analysis of blood motion strives to comprehensively characterise the turbulence by inspecting the energy carried by the vortical structures of the flow following vortex ring formation, a shedding process including vortex stretching and advection[9]. We seek to observe the typical energy decay of kinetic energy (KE) as described in the theory of turbulence[23]. Additionally, we investigate any deviations from this theoretical energy decay along with examining the dissipation rate of KE. Connection between leaflet geometries and turbulence characteristics is underlined. In addition, we analyse and correlate the spatial distributions of the newly introduced concepts of kinetic energy anisotropy and helicity intensity over spherical shells close to the valvular orifice. There has been no previous computational study and comprehensive energy-based analyses that include valve bioprostheses of different designs alongside a comparative assessment with a severe stenotic case. This work significantly contributes to the development of optimally designed valves by thoroughly elucidating the flow-energy-based mechanisms downstream of BioAVs in comparison to those encountered downstream of a severe aortic stenosis.

Spectral analysis and turbulence characteristics

The log-log graphs presented in Fig. 1 (a, b, c) display the distribution of the modal KE at different scalar angular wavenumbers for various time instances considered over systole, represented by thin grey lines. Details on the geometry of three valvular configurations, the stenosed aorta case and the two newly designed bioprosthetic valves (VLth30 and Ulth0), are presented in the Methods section of the first part of the study[9].

In the stenotic case, we note that the trend in the decay of energy as a function of the wavenumber varies depending on the time instant considered as shown by the large difference in E_{u^2} between the dash-dot black line and the solid thick black line, especially for wavenumbers larger than 2,000 rad/m. The maximum non-dimensional modal KE curve (i.e. solid thick line in Fig. 1 (a)) corresponds to the wavenumber spectra at instants t=0.121 s, 0.142 s and 0.172 s. The minimum non-dimensional modal KE curve (cf. dash-dot line in Fig. 1 (a)) corresponds to the spectra at t=0.1 s.

Concerning the VLth30 BioAV case, the log-log plot (see Fig. 1 (b)) shows that the variations in the energy decay over the different time instants is smaller than that noted in the stenotic case. These differences between time instances in E_{u^2} are even smaller in the Ulth0 BioAV case. Indeed, as presented in the first part of the current comprehensive study[9], the Ulth0 valve design leads to very limited leaflet motion after their opening throughout systole and the jet shape downstream remains relatively stable, except for Kelvin-Helmholtz instability (KHI) arising between t=0.12 s and t=0.21 s.

In order to verify whether the logarithmic slope of -5/3 characteristic of the inertial subrange for turbulent flows according to Kolmogorov's theory[23] can be noted, E_{u^2} has been divided by $\kappa^{-5/3}\varepsilon^{2/3}$ and the graphs of the first-order derivative with respect to the wavenumber are presented in Fig. 1 (d, e, g). Additionally, the temporal evolution of the turbulent KE dissipation ε is presented in Fig. 2 (b).

For the stenosed aorta case, the curves of minimum, median and maximum non-dimensional $d\left(\frac{E_{u2}}{\kappa^{-5/3}\varepsilon^{2/3}}\right)/d\kappa$ are almost superimposed on each other. Moreover, these curves follow the universal scaling law predicted by Kolmogorov turbulence theory over a wide range of wavenumbers, i.e. between 2,000 and 20,000 rad/m where $d\left(\frac{E_{u2}}{\kappa^{-5/3}\varepsilon^{2/3}}\right)/d\kappa$ is equal to 0. The self-similarity of vortical structures in the inertial subrange is then, in the stenotic case, observed throughout the whole systolic time interval under consideration. It is worth mentioning that, for the computation of the wavenumber energy spectra, the mode of the log-normal distribution of the correlation function over the points on spherical shells in Fourier space has been taken as the most representative energy level at the considered scalar wavenumber.

In the case of the VLth30 bioprosthesis, the power-law with the exponent of -5/3 characteristic of the inertial subrange for the decay of energy does not appear, except at time instants t = 0.1 s, 0.11 s, 0.12 s and 0.245 s, over a narrow range of wavenumbers (see the video in the supporting information). Conversely, peaks of energy at $\kappa = 5{,}000$ rad/m and $\kappa = 7{,}500$ rad/m are noticeable as exhibited in Fig. 1 (e). For values of κ ranging from 1,000 to 6,500 rad/m, it has been calculated that the minimum, median and maximum values in time of the $E_u^2/\varepsilon^{2/3}$ curve scale as $\kappa^{-5/3}\ln(\kappa)$, $\kappa^{-5/3}\ln(\kappa)$ and $\kappa^{-7/6}$, respectively.

In the Ulth0 BioAV case, the curve of $d\left(\frac{E_{u2}}{\kappa^{-5/3}\varepsilon^{2/3}}\right)/d\kappa$ equals 0 over wavenumbers ranging from 4,000 to 9,000 rad/m for time instances between t = 0.12 s and t = 0.19 s. Interestingly, these instants correspond to the times at which the KHI establishes as discussed in[9]. In Fig. 1 (f), we observe that, for scalar wavenumbers from 1,000 and 6,000 rad/m, the minimum, median and maximum in time of $\frac{E_{u2}}{\varepsilon^{2/3}}$ curve scale as κ^{-2}, $\kappa^{-4/3}$ and $\kappa^{-3/2}$, respectively.

[Figure 1 about here.]

Fig. 2 (a) presents the time evolution of the Kolmogorov length scale derived from the dissipation rate of turbulent KE ε computed over the spherical shells (cf. Fig. 8). This length scale is the smallest in the stenotic case with a value of about 20 μm constant over systole. In the cases of the two valvular bioprostheses, the Kolmogorov length scale is two to four times the value evaluated downstream of the stenosed aorta. Furthermore, as a consequence of the peak in energy dissipation at t=0.15 s (Fig. 2 (b)), the Ulth0 case exhibits a reduction in the Kolmogorov length scale, decreasing from 80 to 40 μm. The Kolmogorov length scale in the VLth30 case ranges from 40 to 50 μm over systole.

The integral length scale $\mathfrak{L}$ is presented in Fig. 2 (c) and was determined by computing the autocorrelation function for each component of the velocity vector $\mathbf{u}$ in physical space. Subsequently, an equivalent autocorrelation function was calculated over points distributed on spherical surfaces and $\mathfrak{L}$ was obtained by computing the L^2-norm of this equivalent autocorrelation function in each direction. In the stenotic case, the time-averaged integral length scale is approximately 2.8 mm while for the two BioAV prostheses, the time-averaged $\mathfrak{L}$ ranges from 4.5 to 5 mm.

[Figure 2 about here.]

Energy distribution

In this section, we investigate the distribution of energy intensity in physical space, i.e. over spherical surfaces, as defined in the Materials and Methods section. We intend to compare the energy levels among the following cases: the stenosed aorta case, the two newly designed bioprosthetic valves (VLth30 and Ulth0) and a bioprosthetic case presented in the study by Gallo *et al.*[13].

With regard to the turbulent KE intensity, we note in Fig. 3 (a) and (e) that the maximum $\mathbb{I}_{u'^2}$ for the three valvular bioprostheses represents 30% of the maximum $\mathbb{I}_{u'^2}$ in the stenosis case. The time-averaged fluctuating energy intensity for the three BioAV cases is one-sixth that of the stenotic case as illustrated in Fig. 4 (e). We also observe from Fig. 4 (a) that the temporal profile shape for the Ulth0 BioAV case is congruent with the BioAV case investigated in Gallo *et al.*, with the exception that, due to differences in the acceleration and deceleration inflow conditions, the green curve of the BioAV studied by Gallo *et al.* is shifted in time relative to the Ulth0 curve.

In regards to the fluctuating enstrophy intensity $\mathbb{I}_{\omega'^2}$, the time-averaged value for the VLth30 valvular case is thrice that of the stenotic case and the Ulth0 BioAV case. The elevated levels of fluctuating enstrophy in the VLth30 case arise from the non-axisymmetric and more pronounced leaflet motion, with a displacement magnitude of approximately 2 *mm* during systole[27,9]. This finding is consistent with the higher levels of streamwise instantaneous vorticity highlighted in the first part of the study[9]. For the VLth30 case, it is worthwhile to note that the times at which a local minimum in the fluctuating enstrophy temporal evolution is found (i.e. t=0.12, 0.156, 0.21, 0.256 s) correspond to the times at which the area at the vena contracta is maximum[9].

Closely related to the notion of vortex stretching is helicity in flows. Helicity is the integral over a volume of interest of the inner product between velocity and vorticity vectors. Helicity plays an important role in the generation and evolution of vortices and it was shown that it tightly connects to the knottedness and the twisting of vortex lines[18,19].

In addition, helicity is known to inhibit the transfer of energy towards smaller scales, since the statistical alignment of velocity and vorticity leads to partial suppression of the non-linear term and to a relatively low dissipation[13]. The results in Fig. 3 (c, d, e) are aligned with this statement. For both the VLth30 and Ulth0 cases, the time-averaged and maximum values of unsigned helicity intensity (III and IV) are 2 to 2.5 times as large as those observed in the stenotic case. Moreover, the curves of signed helicity intensity (Fig. 3(d)) for the VLth30 and Ulth0 BioAVs exhibit peaks with a magnitude 10 times larger than those observed in the stenotic case and in the BioAV case investigated in Gallo *et al.*. As emphasised in the previous section, the logarithmic slope of the three-dimensional wavenumber spectra (represented by the median, maximum, and minimum curves over time) for the two BioAV cases is larger than the -5/3 logarithmic slope predicted by Kolmogorov for isotropic and homogeneous turbulence, which is found to hold though in the stenotic case. This suggests an inhibition of non-linear advection in the energy cascade, likely due to the presence of local helical flow motion, in the region near the bioprosthetic valvular orifice. Finally, it is worth noting in Fig. 3(d) that the signed helicity intensity $\mathbb{I}_{h'^2}$ in the VLth30 case exhibits an average negative value across spherical shells between t=0.1 and t=0.15 s. This indicates the prevalence of counter-clockwise helical structures in the vicinity of the valvular orifice during this time period. In contrast, in the Ulth0 case, the signed helicity intensity remains positive until t=0.2 s, suggesting the dominance of clockwise helical motion. After t=0.15 s, a decrease in $\mathbb{I}_{h'^2}$ is observed, eventually reaching small negative values until t=0.28 s.

[Figure 3 about here.]

Anisotropy in the modal kinetic energy and helicity intensity

In this section, the novel quantities defined in Eq. 27 and Eq. 28 representing the modal KE anisotropy $\mathbb{I}_{p_s}^{\mathsf{flow\ anis}}$ and normalised helicity intensity $\mathbb{I}_{p_s}^{h|_{\mathsf{sph}}}$, respectively, are characterised and correlated through probability density function (PDF) and spatial heatmaps, unrolled by means of a cylindrical projection from the distribution over spherical shells described in the Materials and Methods section.

In Fig. 4 (a), the log-normal PDF fitted to the absolute value of $\mathbb{I}_{p_s}^{\mathsf{flow\ anis}}$ distributed over the spherical surfaces (cf.Fig.8) and evolving in time is presented. We observe that, across all time instances considered between t=0.1 and 0.3 s, the mode of the log-normal distribution for $|\mathbb{I}_{p_s}^{\mathsf{flow\ anis}}|$ in the stenotic case is 35% and 65% higher than the modes of the log-normal distributions in the VLth30 and Ulth0 cases, respectively. In the same figure, the modes for each time instance considered are represented with lozenges and the stenotic case displays a maximum mode value of 9.5% against 7.9% for the VLth30 case and 6% for the Ulth0 case. We can also notice this trend in the PDFs and boxplots of $\mathbb{I}_{p_s}^{\mathsf{flow\ anis}}$ shown in Fig. 4 (b) for the three valvular cases. In fact, the maximum values of $\mathbb{I}_{p_s}^{\mathsf{flow\ anis}}$ equals 136%, 92% and 81.3% for the stenotic, VLth30 and Ulth0 cases, respectively. In Fig. 4 (b), it can be seen that the median value for $\mathbb{I}_{p_s}^{\mathsf{flow\ anis}}$ is positive for the two bioprosthesis cases, with a value of around 1.5% whereas the median value for the stenotic is negative and equal to -2.2%. The asymmetry in the probability distribution of modal KE is indicative of asymmetries in jet flows, which are associated with complex vortex dynamics[9], especially when helicity is non-zero[10]. The skewness of the VLth30 probability density function (PDF) is negative, while that of the stenotic PDF is positive. Both cases exhibit a similar interquartile range (IQR) value of 35%. In contrast, the PDF for the Ulth0 case appears almost symmetric, as emphasised by Corso et al.[9], as a consequence of a triangular jet flow topology with low eccentricity distance throughout systole. The IQR in the Ulth0 case equals 27%.

[Figure 4 about here.]

In Fig. 5, the spatial distribution of the absolute value of the modal KE anisotropy intensity $|\mathbb{I}_{p_s}^{\mathsf{flow\ anis}}|$ (Eq. 27) is presented by unrolling the spherical through a cylindrical projection. The standard deviation σ over the investigated time instances and the time average ($\overline{\circ}$) of $|\mathbb{I}_{p_s}^{\mathsf{flow\ anis}}|$ are compared based on the two-dimensional (α, φ) maps. In the stenotic case, in Fig. 5 (c), we observe that $|\overline{\mathbb{I}_{p_s}^{\mathsf{flow\ anis}}}|$ reaches its maximum, with values ranging from 25% to 40%, at the azimuthal angles corresponding to the locations of commissures 1, 2, and 3 (i.e., at $\alpha \approx$ -120°, -10° and 80°). The standard deviation $\sigma\left(|\mathbb{I}_{p_s}^{\mathsf{flow\ anis}}|\right)$ attains peak values of 15% in the region between commissures 1 and 3. This region corresponds to a zone where low flow velocities and few coherent vortical structures with limited stretching are found[9]. We also notice a region with moderately high values of 5% for $\sigma\left(|\mathbb{I}_{p_s}^{\mathsf{flow\ anis}}|\right)$ at elevation angles $\varphi > 50°$. Concerning the VLth30 BioAV, Fig. 5 (e) and (f) reveal that $\sigma\left(|\mathbb{I}_{p_s}^{\mathsf{flow\ anis}}|\right)$ and $|\overline{\mathbb{I}_{p_s}^{\mathsf{flow\ anis}}}|$ are the largest for $\varphi <$ -50°. In addition, peak values in the standard deviation of absolute value of modal KE anisotropy, reaching 15%, are found at azimuthal angles of -150°, -30° and 90°. We observe that these peaks are aligned with the position of the three posts of the BioAV ring (see Fig.2 of the paper discussing the first part of the study for the description of the BioAV geometries[9]). With respect to the Ulth0 bioprosthesis, the values for the spatial distribution of $\sigma\left(|\mathbb{I}_{p_s}^{\mathsf{flow\ anis}}|\right)$ and $|\overline{\mathbb{I}_{p_s}^{\mathsf{flow\ anis}}}|$ are noticeably lower, as previously indicated based on the PDFs and the modes of the fitted log-normal distribution. However, peaks in the time-averaged absolute value of modal KE anisotropy $|\overline{\mathbb{I}_{p_s}^{\mathsf{flow\ anis}}}|$ can be observed in Fig. 5 (i). Akin to the VLth30 case, these peaks are positioned at angles α aligned with the positions of the valvular ring posts.

[Figure 5 about here.]

Fig. 6 presents the comparison and point-to-point correlation between the unrolled maps of time-averaged modal KE anisotropy and normalised helicity intensity. The interest in conducting such a correlation lies in the findings presented by Gallo *et al.*[13], which reveal a strong linear relationship between phase-averaged and fluctuating helicity and KE. In the study by Gallo *et al.*, the correlation was established based on volume-averaged energy and helicity over the cardiac cycle.

In Fig. 6 (b, f, j), the heatmaps of time-averaged normalised helicity intensity are displayed. These maps suggest that the spatial distribution of $\overline{\mathbb{I}_{p_s}^{h|\mathsf{sph}}}$ is inversely proportional to the spatial distribution of $\overline{|\mathbb{I}_{p_s}^{\mathsf{flow\ anis}}|}$, as depicted in the maps shown in Fig. 6 (a, e, i). In order to conduct a point-to-point correlation for the three valvular cases, a non-linear least-square regression problem is solved. To achieve this, the points on the (α, φ) maps are divided into two sets: one is the training set used for fitting the coefficients A and B in the power-law equation of the form $\overline{|\mathbb{I}_{p_s}^{\mathsf{flow\ anis}}|} = A \left[\overline{\mathbb{I}_{p_s}^{h|\mathsf{sph}}}\right]^B$ and the other is the testing set used to evaluate the prediction accuracy. The latter is assessed through the coefficient of determination (R^2)[7,8,27]. From Fig. 6 (c, g, k), it can be noted that, for the three valve configurations, $\overline{|\mathbb{I}_{p_s}^{\mathsf{flow\ anis}}|}$ inversely correlates with $\overline{\mathbb{I}_{p_s}^{h|\mathsf{sph}}}$ as demonstrated by the negative fitted exponent B (cf. Table 1 in the supplementary information). The accuracy of the regression from R^2 evaluated on the training (Fig. 6 (g)) and testing (Fig. 6 (h)) data points of the heatmaps is the highest with a value of about 0.75 in the VLth30 BioAV case. This valve design leads to non-axisymmetric leaflet motions with displacement magnitude of about 2 mm during systole (see supplementary material of[9]). The eccentricity of the jet calculated in a proximal cross-section as well as the area at the vena contracta is also evaluated in[9] and it has been shown that the leaflet motions produce stronger levels of vortex stretching magnitude as compared to the Ulth0 BioAV case, whose leaflets are almost immobile throughout systole. The latter case exhibits a low coefficient of determination R^2 of 0.1 based on both the training and testing data points from the heatmaps or spherical shells, indicating a weaker anti-correlation between modal KE anisotropy and normalised helicity intensity. Regarding the stenotic case, the correlation accuracy on the training dataset is moderate with $R^2 = 0.43$ (see Fig. 6 (c)) while the coefficient of determination drops to 0.1 on the testing data points (Fig. 6 (d)).

The variation in the prediction accuracy and strength of correlation among the three valvular cases under examination is an interesting point to analyse. In fact, as stated by Gallo *et* *al.*[13], the role of helicity in the generation and evolution of turbulence may depend on the topology of the flow and vortices, namely dependent on the vortex stretching process. In the first part of this broad study[9], we highlight three different jet flow topologies connected to the valvular orifice architecture. It can then be postulated that flow asymmetries introduced by moving leaflets, as highlighted in the VLth30 case by the presence of a jet with high velocities in a proximal cross-section[9], which changes shape over time and exhibits varying eccentricity, result in higher levels of KE anisotropy close to the orifice and a stronger negative correlation with normalised helicity intensity. Finally, it is worth noting for both BioAV cases, similarly to what was observed for $\overline{|\mathbb{I}_{p_s}^{\mathsf{flow\ anis}}|}$ and $\sigma\left(|\mathbb{I}_{p_s}^{\mathsf{flow\ anis}}|\right)$, high values of $\overline{\mathbb{I}_{p_s}^{h|_{\mathsf{sph}}}}$ are found at azimuthal angles where the three valve ring posts (indicated by the letter P in Fig. 6) are located.

[Figure 6 about here.]

Leaflet dynamics analysis and anisotropy in the valve motion

Since we previously highlighted the potential impact of moving leaflets on the degree of correlation between KE anisotropy intensity and normalised helicity intensity, in Fig. 7 (a, b, e, f), we closely examine the KE carried by the moving structural components of the two BioAVs.

As demonstrated in Fig. 7 (a) and (b), the standard deviation of leaflet displacement magnitude over time in the VLth30 case is four times that in the Ulth0 case, as previously highlighted in the first part of the study[9]. The standard deviation of the displacement magnitude in the supporting ring of the BioAVs is highest at the extremity of the three posts. In the initial part of the study[9], hairpin-like vortices were observed near the three posts as a consequence of the motion of the leaflets and posts, particularly when the gap between the leaflets and the ring post widens.

In Fig. 7 (b), the spatial distribution of the standard deviation of biomechanical KE anisotropy for the VLth30 case shows strong variation amongst the three leaflets while for the Ulth0 BioAV, $\sigma\left(\mathbb{I}_{p_s}^{\text{flow anis}}\right)_{\text{norm}}$ is more uniformly distributed. With a view to establishing a correlation between the flow and structural anisotropy intensity, we have plotted the graphs depicting the standard deviation of flow modal KE anisotropy and biomechanical KE anisotropy. These values are averaged over the elevation angles φ and normalised to range from 0 to 1, as shown in Fig. 7 (c) and (g). The cross-correlation function of the curves in the graphs of Fig. 7 (c) and (g) has been calculated and is presented in Fig. 7 (d) and (h). It is worth noting that, in the case of the VLth30 BioAV, the graph indicates a strong correlation between flow and biomechanical anisotropy, as the cross-correlation function reaches its peak at an azimuthal shift of 0°. In the case of the Ulth0 BioAV, the cross-correlation function in Fig.7 (h) indicates a relatively strong correlation, with peak values occurring at azimuthal shifts ranging from -10° to 0°. However, the curves in Fig.7 (g) suggest an inverse correlation, as the minima in $\sigma\left(\mathbb{I}_{p_s}^{\text{flow anis}}\right)_{\text{norm}}$ align with the maxima in $\sigma\left(\mathbb{I}_{p_m}^{\text{struct anis}}\right)_{\text{norm}}$.

[Figure 7 about here.]

Outlook

The findings emphasise the influence of valve architecture on turbulence characteristics in the ascending aorta near the valvular orifice, with aortic stenosis serving as the benchmark worst-case scenario. The complex interplay among energy, helicity, leaflet motion and KE anisotropy is discussed, underscoring the significance of the present work in evaluating BioAV performance and advancing the development of energy-efficient BioAVs.

In fact, the investigation of flow disturbances associated with turbulence, conducted in this second part of a comprehensive study, relies on advanced energy-based analyses. These analyses include a dedicated three-dimensional spectral analysis and the introduction of new quantities, namely the modal and biomechanical KE anisotropy.

The detailed two-part computational study lays the foundation for a comprehensive set of analyses, forming a robust platform for the development of innovative and personalised valve designs. These designs aim to reduce the adverse consequences linked to aortic valve replacement.

Methods

The present study constitutes the second part of a comprehensive investigation. Therefore, for information regarding the geometry of the aortic model, the two valvular bioprostheses and aortic stenosis along with details about the numerical setups, solving methods and experimental validation of the solvers, readers are referred to the article that presents the first part of this extensive study[9].

Spectral analysis on the blood motion

The spectral analysis proposed in this study relies upon the incompressible Navier-Stokes equations expressed in Fourier space[14]:

$$\boldsymbol{\kappa} \cdot \hat{\mathbf{u}}(\boldsymbol{\kappa}) = 0, \tag{1}$$

with $\boldsymbol{\kappa}$, the angular wavenumber vector, $\mathbf{u}$, the instantaneous flow velocity vector and $\hat{\mathbf{u}}$, the Fourier modes of $\mathbf{u}$.

$$\frac{d\hat{\mathbf{u}}(\boldsymbol{\kappa})}{dt} + i \sum_{\boldsymbol{\kappa}'} \{\boldsymbol{\kappa} \cdot \hat{\mathbf{u}}(\boldsymbol{\kappa} - \boldsymbol{\kappa}')\} \hat{\mathbf{u}}(\boldsymbol{\kappa}') = -i\boldsymbol{\kappa}\, \hat{p}(\boldsymbol{\kappa}) - \nu \kappa^2 \hat{\mathbf{u}}(\kappa), \tag{2}$$

with $i = \sqrt{-1}$, ν, the kinematic viscosity and $\hat{p}(\boldsymbol{\kappa})$, the modal kinematic pressure.
From these spectral equations, after eliminating the pressure term by projecting the advective term on the plane of incompressibility[16], an equation for the dynamics of the modal KE can be derived by taking the inner product of Eq. 2 with the complex-conjugate $\hat{\mathbf{u}}^*(\kappa)$ adding the complex-conjugate to the resultant equation. As a result, we obtain the following equations[14,23]:

$$\frac{d}{dt}\hat{E}_{u^2}(\boldsymbol{\kappa}) = \underbrace{\sum_{\boldsymbol{\kappa}'} \mathfrak{Im}\left(\{\boldsymbol{\kappa}\cdot\hat{\mathbf{u}}(\boldsymbol{\kappa}-\boldsymbol{\kappa}')\}\{\hat{\mathbf{u}}(\boldsymbol{\kappa}')\cdot\hat{\mathbf{u}}^*(\boldsymbol{\kappa})\}\right)}_{\hat{T}_{u^2}(\boldsymbol{\kappa})} - \underbrace{2\nu\kappa^2\hat{E}_{u^2}(\boldsymbol{\kappa})}_{\hat{D}_{u^2}(\boldsymbol{\kappa})}, \tag{3}$$

with $\hat{E}_{u^2}$, the modal kinetic energy, $\hat{T}_{u^2}$, the rate of kinetic energy transfer to the modal kinetic energy due to non-linearity and $\hat{D}_{u^2}$, the dissipation rate of modal kinetic energy through viscous effects. $\mathfrak{Im}$ is the imaginary part.

It is possible to calculate the total dissipation rate ε by summing $\hat{D}_{u^2}(\boldsymbol{\kappa})$ over the wavenumber. This dissipation ε is used to estimate the Kolmogorov microscales[23].

Furthermore, it is suggested in[12] that for non-isotropic turbulence, the spatial velocity function and the spectrum function be expressed in terms of a single scalar distance r and wavenumber κ, respectively, by taking mean values of the functions over spherical surfaces given by radius r = constant in physical space and κ = constant in Fourier space.

This way, the kinetic energy of the Fourier modes $\hat{E}_{u^2}$ of the three-dimensional and anisotropic velocity field obtained from the simulations is calculated by sampling the velocity components on points distributed over spherical shells centred around a point on the centreline of the ascending aorta (see Fig. 8). A sequence of velocity values ($\mathbf{u}_s$) is then defined over each radius of the sphere of points. The points on each spherical shell (i.e. at r = constant) are obtained by distributing them with a constant increment in both azimuthal and elevation angles of 30 degrees, resulting in a set of 122 equidistant points on the shell, spaced at an arc length of $\frac{\pi r}{6}$.

[Figure 8 about here.]

A one-dimensional formulation of the continuous Fourier transform operator on a finite interval $(0, \mathcal{L})$ allowing to express the Fourier coefficients of the continuous three-dimensional velocity field $\mathbf{u}(\boldsymbol{x})$ is defined as follows[23]:

$$\mathcal{F}_{\kappa}\{\mathbf{u}(r)\} = \hat{\mathbf{u}}(\kappa) = \frac{1}{\mathcal{L}}\int_0^{\mathcal{L}} \mathbf{u}(r)\exp\left(-i\kappa r\right)dr, \tag{4}$$

with r, the radial coordinate along each radius of the sphere of points; $\mathcal{L}$, the radius of the largest spherical surface used for the sampling. The largest radius is equal to 10 mm and 11.5 mm for the aortic stenosis and bioprosthesis cases, respectively. It is noteworthy that the three-dimensional formulation of the Fourier operator is reduced to the above one-dimensional formulation by integrating along each radius of the sphere of points and by considering $\boldsymbol{\kappa} \cdot \boldsymbol{x} = \kappa r$[23]. It is also important to note that the calculation of Fourier modes implies the periodicity in the velocity field $\mathbf{u}(r)$. However, if we consider the integral length scale $\mathfrak{L}$, the effects of this artificially imposed periodicity vanish as $\frac{\mathcal{L}}{\mathfrak{L}}$ tends to infinity[23].
The corresponding discrete Fourier transform (DFT) using a fast Fourier transform (FFT) algorithm[11] is performed based on the instantaneous velocity field $\mathbf{u}$ sampled on a sequence of points distributed over spherical shells $(\mathbf{u}_s)$ as shown in Fig. 8. The centre of the spherical shells is positioned on the centreline of the straight aorta at a distance of 12.5 mm and 8 mm from the sino-tubular junction in the stenotic and BioAV cases, respectively. The DFT is then expressed as:

$$\hat{\mathbf{u}}_k = \frac{1}{(N-1)\Delta r} \sum_{s=0}^{N-1} \mathbf{u}_s \exp\left(\frac{-i2\pi ks}{N}\right) \Delta r, \tag{5}$$

with $k = 0, ..., N-1$. N is the number of points taken over each radius of the spherical distribution of points and is equal to 82 and 48 for the stenotic and BioAV cases, respectively. Δr, is the distance between two consecutive spherical shells and is equal to 125 μm for the stenosis case and 250 μm for the aortic bioprosthesis cases. Each entry of the sequence of scalar angular wavenumbers κ corresponding to the sequence $(\hat{\mathbf{u}}_k)$ is $\kappa_k = \frac{(k+1)}{N}\frac{2\pi}{\Delta r}$ leading to $\hat{\mathbf{u}}(\kappa) = \hat{\mathbf{u}}_k$.

In order to avoid the presence of aliases in the spectrum obtained out of the FFT operation and considering the symmetry of the spectrum given the real-valued velocity sequence $(\mathbf{u}_s)$, the values of $\hat{\mathbf{u}}(\kappa)$ above the folding wavenumber $\kappa_f = \frac{\pi}{\Delta r}$ are discarded. These correspond to the entries $\hat{\mathbf{u}}_k$ with index $k > \lfloor \frac{N+1}{2} \rfloor = N'$.

The normalised and discrete first-order autocorrelation function over each radius of the spherical distribution of points is then calculated from the modal velocity vector $\hat{\mathbf{u}}_k(\hat{u}_{x\,k}, \hat{u}_{y\,k}, \hat{u}_{z\,k})$:

$$\hat{\mathcal{R}}_I^{u_j u_j} = \frac{1}{|\hat{\mathcal{R}}_0^{u_j u_j}|} \sum_{n=0}^{N'-m-1} \left(\hat{u}_{j\,n+I}\ \hat{u}_{j\,n}^{\,*} \right), \tag{6}$$

with $j = (x, y, z)$, $m = 1, ..., 2N' - 1$, the index $I \in [-N', N']$ and the range of indices I considered for $\hat{\mathcal{R}}^{u_i u_i}$ is $[0, N']$.

By inspecting the distribution of the correlation function over the points of each spherical shell, we note a log-normal distribution. Therefore, in order to have the most representative value of the autocorrelation function $\hat{\mathcal{R}}^{u_j u_j}$ over each spherical surface, the mode of this distribution instead of the previously mentioned expected value[12] has been employed to compute an equivalent autocorrelation function $\hat{\mathcal{R}}^{u_j u_j}$ so that the latter is dependent on a single scalar wavenumber κ for each spherical shell. The equivalent correlation function (coming from the mode of the log-normal distribution) is then defined as:

$$\hat{\mathcal{R}}^{u_j u_j}\big|_{\mathsf{eq}} = \exp(M^{\mathcal{R}} - \Sigma^{\mathcal{R}}), \tag{7}$$

$M^{\mathcal{R}} = \log\left[\frac{\langle \hat{\mathcal{R}}^{u_j u_j}|_{\mathsf{sph}}\rangle}{\sqrt{\langle \hat{\mathcal{R}}^{u_j u_j}|_{\mathsf{sph}}\rangle^2 + \mu_2(\hat{\mathcal{R}}^{u_j u_j}|_{\mathsf{sph}})}}\right]$, $\Sigma^{\mathcal{R}} = \log\left[1 + \frac{\mu_2(\hat{\mathcal{R}}^{u_j u_j}|_{\mathsf{sph}})}{\langle \hat{\mathcal{R}}^{u_j u_j}|_{\mathsf{sph}}\rangle^2}\right]$, with $\langle \hat{\mathcal{R}}^{u_j u_j}|_{\mathsf{sph}}\rangle$; the expected value and $\mu_2(\hat{\mathcal{R}}^{u_j u_j}|_{\mathsf{sph}})$; the variance of $\hat{\mathcal{R}}^{u_j u_j}$ over the 122 points of each spherical shell.

Finally, each term of Eq. 3 are calculated based on the one-dimensional DFT of the velocity field sampled on points distributed over spherical shells and based on the ensuing equivalent autocorrelation function $\hat{\mathcal{R}}^{u_j u_j}\big|_{\mathsf{eq}}$. Therefore, the equivalent modal KE $\hat{E}_{u^2}(\kappa)$ reads:

$$\hat{E}_{u^2}(\kappa) = \frac{1}{2}\left(\hat{\mathcal{R}}^{u_x u_x}\big|_{\mathsf{eq}} + \hat{\mathcal{R}}^{u_y u_y}\big|_{\mathsf{eq}} + \hat{\mathcal{R}}^{u_z u_z}\big|_{\mathsf{eq}} \right). \tag{8}$$

The rate of modal KE transfer $\hat{T}_{u^2}(\kappa)$ is computed as follows:

$$\hat{T}_{u^2}(\kappa) = \frac{1}{2}\left(\hat{T}^{u_x^2}\big|_{\mathsf{eq}} + \hat{T}^{u_y^2}\big|_{\mathsf{eq}} + \hat{T}^{u_z^2}\big|_{\mathsf{eq}} \right), \tag{9}$$

where

$$\hat{T}^{u_j^2}(\kappa) = \sum_{\kappa'} \mathfrak{Im}\left(\{\kappa \cdot \hat{u}_j(\kappa - \kappa')\}\{\hat{u}_j(\kappa') \cdot \hat{u}_j^{\,*}(\kappa)\} \right), \tag{10}$$

and

$$\hat{T}^{u_j^2}\Big|_{\mathsf{eq}} = \exp(M^T - \Sigma^T), \tag{11}$$

with $M^T = \log\left[\frac{\langle \hat{T}^{u_j^2}|_{\mathsf{sph}}\rangle}{\sqrt{\langle \hat{T}^{u_j^2}|_{\mathsf{sph}}\rangle^2 + \mu_2(\hat{T}^{u_j^2}|_{\mathsf{sph}})}}\right]$, $\Sigma^T = \log\left[1 + \frac{\mu_2(\hat{T}^{u_j^2}|_{\mathsf{sph}})}{\langle \hat{T}^{u_j^2}|_{\mathsf{sph}}\rangle^2}\right]$.

Kinetic energy, enstrophy and helicity in blood flow

In order to obtain the fluctuations in the velocity $\mathbf{u}'$ and vorticity $\boldsymbol{\omega}'$ fields of blood flow, a Reynolds decomposition is performed. With a view of removing the effect of the temporal periodicity in the leaflet motion on the downstream flow, the time-averaged (over all the considered time-steps) velocity and vorticity fields are combined with the velocity and vorticity field phase-averaged at the main frequencies extracted from the leaflet motion analysis[9]. This decomposition is akin to performing a triple decomposition[15] and leads to the following formulation for the fluctuating vector fields:

$$\mathbf{u}' = \mathbf{u} - \frac{1}{2}\mathbf{U} - \frac{1}{2}\mathbf{U}_{\mathsf{periodic}} = \mathbf{u} - \underbrace{\frac{1}{2}\left[\frac{1}{T}\int_0^T \mathbf{u}\, dt + \frac{1}{N}\sum_N \mathbf{u}(t + \frac{N}{f_{\mathsf{mech}}})\right]}_{\mathbf{U}^{\mathsf{tot}}}, \tag{12}$$

with $\mathbf{U}$, the velocity vector field averaged over the whole simulated systole T; $\mathbf{U}_{\mathsf{periodic}}$, the phase-averaged velocity field at frequencies f_{mech} evaluated from the leaflet mechanics characterisation[9]. The average between these two time-averaged velocity fields gives $\mathbf{U}^{\mathsf{tot}}$. Likewise, the fluctuating vorticity field is given by:

$$\boldsymbol{\omega}' = \boldsymbol{\omega} - \frac{1}{2}\boldsymbol{\Omega} - \frac{1}{2}\boldsymbol{\Omega}_{\mathsf{periodic}} = \boldsymbol{\omega} - \underbrace{\frac{1}{2}\left[\frac{1}{T}\int_0^T \boldsymbol{\omega}\, dt + \frac{1}{N}\sum_N \boldsymbol{\omega}(t + \frac{N}{f_{\mathsf{mech}}})\right]}_{\boldsymbol{\Omega}^{\mathsf{tot}}}, \tag{13}$$

with $\boldsymbol{\omega} = \nabla \times \mathbf{u}$, the instantaneous vorticity field; $\boldsymbol{\Omega}$, the mean vorticity vector field time-averaged over the whole systole, $\boldsymbol{\Omega}_{\mathsf{periodic}}$, the vorticity field phase-averaged at frequencies evaluated from the leaflet mechanics characterisation[9] and $\boldsymbol{\Omega}^{\mathsf{tot}}$, the arithmetic average of the latter two vorticity fields averaged in time.

The terms accounting for the periodicity in the flow field due to the periodic leaflet motion ($\mathbf{u}_{\mathsf{periodic}}$ and $\boldsymbol{\omega}_{\mathsf{periodic}}$) are obviously null in the stenotic case and in the case where the leaflets are not moving.

The total turbulent KE, fluctuating enstrophy and fluctuating helicity are given by:

$$TE_{u'^2} = \int_r \frac{1}{2} \left(\mathbf{u}'(r) \cdot \mathbf{u}'(r)\right) dr, \tag{14}$$

$$TE_{\omega'^2} = \int_r \frac{1}{2} \left(\boldsymbol{\omega}'(r) \cdot \boldsymbol{\omega}'(r)\right) dr, \tag{15}$$

$$TE_{|h'|} = \int_r \frac{1}{2} |\mathbf{u}'(r) \cdot \boldsymbol{\omega}'(r)| dr, \tag{16}$$

$$TE_{h'} = \int_r \frac{1}{2} \left(\mathbf{u}'(r) \cdot \boldsymbol{\omega}'(r)\right) dr, \tag{17}$$

with r, the coordinate along each radius corresponding to the radius from the centre point of the spherical distribution of points defined in the spectral analysis section.

The mean KE, enstrophy and helicity are defined as:

$$TE_{U^2} = \int_r \frac{1}{2} \left(\mathbf{U}^{\mathsf{tot}}(r) \cdot \mathbf{U}^{\mathsf{tot}}(r)\right) dr, \tag{18}$$

$$TE_{\Omega^2} = \int_r \frac{1}{2} \left(\boldsymbol{\Omega}^{\mathsf{tot}}(r) \cdot \boldsymbol{\Omega}^{\mathsf{tot}}(r)\right) dr, \tag{19}$$

$$TE_{|H|} = \int_r \frac{1}{2} |\mathbf{U}^{\mathsf{tot}}(r) \cdot \boldsymbol{\Omega}^{\mathsf{tot}}(r)| dr, \tag{20}$$

$$TE_{H} = \int_r \frac{1}{2} \left(\mathbf{U}^{\mathsf{tot}}(r) \cdot \boldsymbol{\Omega}^{\mathsf{tot}}(r)\right) dr. \tag{21}$$

The turbulence intensity $\mathbb{I}_{u'^2}$ (Eq. 22), intensity of fluctuating enstrophy $\mathbb{I}_{\omega'^2}$ (Eq. 23), intensity of unsigned fluctuating helicity $\mathbb{I}_{|h'|}$ (Eq. 24) and intensity of signed fluctuating helicity $\mathbb{I}_{h'}$ (Eq. 25) are calculated by taking the ratio of the aforementioned fluctuating and mean quantity fields:

$$\mathbb{I}_{u'^2} = \frac{TE_{u'^2}}{TE_{U^2}} \tag{22}$$

$$\mathbb{I}_{\omega'^2} = \frac{TE_{\omega'^2}}{TE_{\Omega^2}} \tag{23}$$

$$\mathbb{I}_{|h'|} = \frac{TE_{|h'|}}{TE_{|H|}} \tag{24}$$

$$\mathbb{I}_{h'} = \frac{TE_{h'}}{TE_{H}} \tag{25}$$

Akin to the calculation of the equivalent autocorrelation function $\hat{\mathcal{R}}^{u_j u_j}$ and the corresponding modal KE $\hat{E}_{u^2}$, we compute an equivalent value for the foregoing intensity fields at each time instance under consideration. This equivalent value represents the most representative intensity field value over the 122 points of the spherical shells and it is determined by taking the mode of the log-normal distribution (cf. Eq. 7).

Flow modal kinetic energy and helicity intensity

The total flow KE $\mathcal{K}_{p_s}$ for each point p_s of the spherical shell is calculated from the normalised and discrete first-order autocorrelation function as follows:

$$\mathcal{K}_{p_s} = \frac{1}{2} \sum_j \int_\kappa \hat{\mathcal{R}}^{u_j u_j}\big|_{\mathsf{sph}} \, d\kappa, \tag{26}$$

with $j = (x, y, z)$ and $p_s = 1, ..., 122$, which corresponds to the index of each point on the spherical shell. The numerical integration is performed using the trapezoidal rule.

The flow modal KE anisotropy $\mathbb{I}_{p_s}^{\mathsf{flow\ anis}}$ over a spherical region close to the aortic orifice is thus defined as:

$$\mathbb{I}_{p_s}^{\mathsf{flow\ anis}} = \frac{\mathcal{K}_{p_s} - \langle \mathcal{K}_{p_s} \rangle}{\langle \mathcal{K}_{p_s} \rangle} \times 100, \tag{27}$$

with $\langle \cdot \rangle$, the average operator over the 122 points of the spherical shell.

Similarly, a normalised helicity intensity $\mathbb{I}_{p_s}^{h|_{\mathsf{sph}}}$ is computed along each radial direction of the spherical shells from the instantaneous helicity intensity field through the following equation:

$$\frac{\mathbb{I}_{p_s}^{h|_{\mathsf{sph}}}}{100} = \frac{\int_r \frac{1}{2} \left(\mathbf{u}(r) \cdot \boldsymbol{\omega}(r) \right) \ dr}{\langle \int_r \frac{1}{2} \left(\mathbf{u}(r) \cdot \boldsymbol{\omega}(r) \right) \ dr \rangle} = \frac{TE_h \big|_{\mathsf{sph}}}{\langle TE_h \big|_{\mathsf{sph}} \rangle} = \frac{\mathbb{I}_h \big|_{\mathsf{sph}}}{\langle \mathbb{I}_h \big|_{\mathsf{sph}} \rangle}. \tag{28}$$

Anisotropy in leaflet and ring kinetic energy

The KE computed at the mesh points p_m located at the leaflet or ring interfaces of the simulated bioprosthetic valve motion is expressed as:

$$KE_{p_m}^{\mathsf{struct}} = \frac{1}{2} \sum_j \mathsf{v}_j^2|_{\mathsf{int}}, \tag{29}$$

with $\mathsf{v}_j|_{\mathsf{int}}$, the $\mathrm{j^{th}}$ velocity component of the structure at the fluid-solid interface (int), which is equal to the flow velocity at the interface by virtue of the velocity continuity condition.

The KE anisotropy $\mathbb{I}_{p_m}^{\mathsf{struct\ anis}}$ in the structure (ring and leaflet) is then defined as:

$$\frac{\mathbb{I}_{p_m}^{\mathsf{struct\ anis}}}{100} = \left[\frac{KE_{p_m}^{\mathsf{struct}} - \langle KE_{p_m}^{\mathsf{struct}} \rangle}{\langle KE_{p_m}^{\mathsf{struct}} \rangle} \right] \left(\mathbf{p}^{\mathsf{struct}} \cdot \mathbf{n}^{\mathsf{struct}} \right), \tag{30}$$

with $\mathbf{p}^{\mathsf{struct}}$, the coordinates of mesh points of the considered structure (leaflet or ring) and $\mathbf{n}^{\mathsf{struct}}$, the outward normal vector to the considered mesh point of the structure. The operator $\langle \cdot \rangle$ corresponds to the average over the different mesh points of the structure.

Acknowledgements

This work was supported by the computational resources from the Swiss National Supercomputing Centre (CSCS) under project IDs c12, s1012 and sm56.

Author contribution

P. Corso: Conceptualisation, Data curation, Formal analysis, Interpretation of the results, Investigation, Methodology, Software, Visualisation, Writing - original draft. **D. Obrist:** Funding acquisition, Input on the results and on the original draft.

Declaration of competing interest

The authors declare that they have no known competing financial interests or personal relationships that could have appeared to influence the work reported in this paper.

Data and materials availability

All data and materials needed to evaluate the conclusions of this paper are present in the main text or supplementary materials. Processable data files can be obtained from the first author.

References

1. Aluru J. S., Barsouk A., Saginala K., Rawla P., Barsouk A., *Valvular Heart Disease Epidemiology*, Medical Sciences, 10, 2022.

2. Bailoor S., Seo J.-H., Dasi L.,*et al. A computational study of the hemodynamics of bioprosthetic aortic valves with reduced leaflet motion*, J. of Biomechanics, 120, 2021.

3. Baumgartner H., Falk V., Bax J. J., De Bonis M., Hamm C., Holm P. J., Lung B., Lancellotti P., Lansac E., Rodriguez Muñoz D., Rosenhek R., Sjögren J., Tornos Mas P., Vahanian A., Walther T., Wendler O., Windecker S., Zamorano J. L. 2017 ESC/EACTS Guidelines for the management of valvular heart disease. European Heart J. 38(36):2739–2791, 2017.

4. Becsek B., Pietrasanta L. and Obrist D., *Turbulent Systolic Flow Downstream of a Bioprosthetic Aortic Valve: Velocity Spectra, Wall Shear Stresses, and Turbulent Dissipation Rates*, Front. in physiol. 11:539-575, 2020.

5. Caballero A.D., Laín S.J.C.E., *A review on computational fluid dynamics modelling in human thoracic aorta*, Cardiovasc. Engng Technol., 4(2):103–130, 2013.

6. Corso P., Gülan U., Cohrs N., *et al.*, *Comprehensive In Vitro Study of the Flow Past Two Transcatheter Aortic Valves: Comparison with a Severe Stenotic Case*, Ann. Biomed. Eng., 47(11):2241-2257, 2019.

7. Corso P., Giannakopoulos G., Gulan U., *et al.*, *A Novel Estimation Approach of Pressure Gradient and Haemodynamic Stresses as Indicators of Pathological Aortic Flow Using Subvoxel Modelling*, IEEE Trans. Biomed. Eng., 68(3):980-991, 2021.

8. Corso P., Walheim J., Dillinger H., *et al.*, *Toward an accurate estimation of wall shear stress from 4D flow magnetic resonance downstream of a severe stenosis*, Magn. Res. Med. 86(3):1531-1543, 2021.

9. Corso P., Obrist D.,*OOn the role of aortic valve architecture for physiological haemodynamics and valve replacement. Part I: flow topology and vortex dynamics*, 2023.

10. Davidson P., *Turbulence: An Introduction for Scientists and Engineers - 2nd Edition*, Oxford University Press, 2015.

11. Frigo M. and Johnson S. G., *The Design and Implementation of FFTW3*, Proceedings of the IEEE, 93(2):216–231, 2005.

12. Frost W., Moulden T. H., *Handbook of Turbulence: volume 1 - Fundamentals and Applications*, Plenum Press, 1977

13. Gallo D., Morbiducci U., de Tullio M. D., *On the unexplored relationship between kinetic energy and helicity in prosthetic heart valves hemodynamics*, Int. J. Eng. Science, 117, 2022.

14. Gupta A., Jayaram R., Chaterjee A. G., *et al.*,*Energy and enstrophy spectra and fluxes for the inertial-dissipation range of two-dimensional turbulence*, Physical Review E, 100, 2019.

15. Hussain A. K. M. F., Reynolds W. C., *The mechanics of an organized wave in turbulent shear flow*. J. Fluid Mech., 41(2):241-258, 1970.

16. Lesieur M. *Turbulence in Fluids: Fourier Analysis of Homogeneous Turbulence*, Springer Dordrecht, 3rd Edition, 1997.

17. Lindman B. R., Clavel M.-A., Mathieu P., Lung B., Lancellotti P., Otto C. M., Pibarot Ph. *Calcific aortic stenosis*. Nature Reviews Disease Primers 2, 2016.

18. Moffatt, H. K., *The degree of knottedness of tangled vortex lines*. J. Fluid Mech., 36: 117-129, 1969.

19. Moffat H. K., Tsinober A., *Helicity in laminar and turbulent flow*, Ann. Rev. Fluid Mech., 24:281-312, 1992.

20. Morbiducci U., Ponzini R., Rizzo G., *et al.*, *Mechanistic insight into the physiological relevance of helical blood flow in the human aorta: An in vivo study*, Biomechanics and Modeling in Mechanobiology, 10:339-355, 2011.

21. Nguyen V., Michel M., Eltchaninoff H., *et al.*, *Implementation of Transcatheter Aortic Valve Replacement in France*, J. Am. College Card., 71(15), 2018.

22. Kitware and Inc. *VTK User's Guide* Kitware Inc., 11^{th} edition, 3 2010. ISBN 978-1930934238.

23. Pope S. B., *Turbulent Flows*, Cambridge University Press, 2000.

24. Pujari S. H., Agasthi P. Aortic Stenosis. [Updated 2022 Apr 14]. In: StatPearls [Internet]. Treasure Island (FL): StatPearls Publishing; 2022 Jan-. Available from: https://www.ncbi.nlm.nih.gov/books/NBK557628/

25. Sotiropoulos F., Le T. B., Gilmanov, A. *Fluid mechanics of heart valves and their replacements*. Annual Review of Fluid Mechanics 48, 259–283, 2016.

26. Townsend A. A., *Entrainment and the structure of turbulent flow*. J. Fluid Mech., 41:13-46, 1970.

27. Tsolaki E., Corso P., Zboray R., *et al.*, *Multiscale multimodal characterization and simulation of structural alterations in failed bioprosthetic heart valves*. Acta Biomaterialia, 169:138-154, 2023.

28. Varghese S. S., Frankel S. H., Fischer P., . *Direct numerical simulation of stenotic flows. Part 1. Steady flow*, J. Fluid Mech., 582:253-280, 2007.

29. Yoganathan A. J., He S., Jones S. C. *Fluid mechanics of heart valves.* Annu. Rev. Biomed. Eng.,6:331–362, 2004.

List of Figures

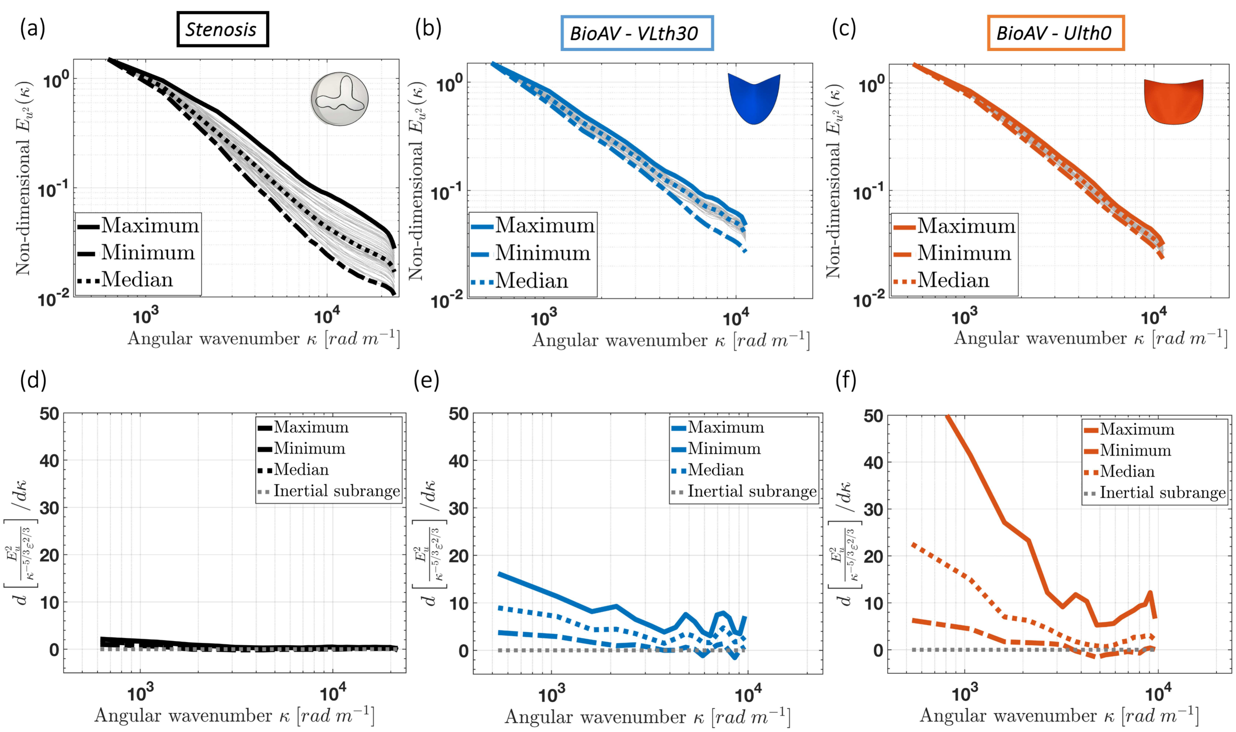

Figure 1: Three-dimensional wavenumber spectra of kinetic energy for the three valvular cases are shown in (a), (b) and (c). These spectra represent the spectral curve for all the considered time instances between t = 0.1 and t = 0.3 s, highlighting the maximum, minimum, and median values at each scalar wavenumber. (d), (e), and (f) display the derivative of the modal KE with respect to the angular wavenumber to determine whether the well-known -5/3 power-law decay is observed in the inertial subrange.

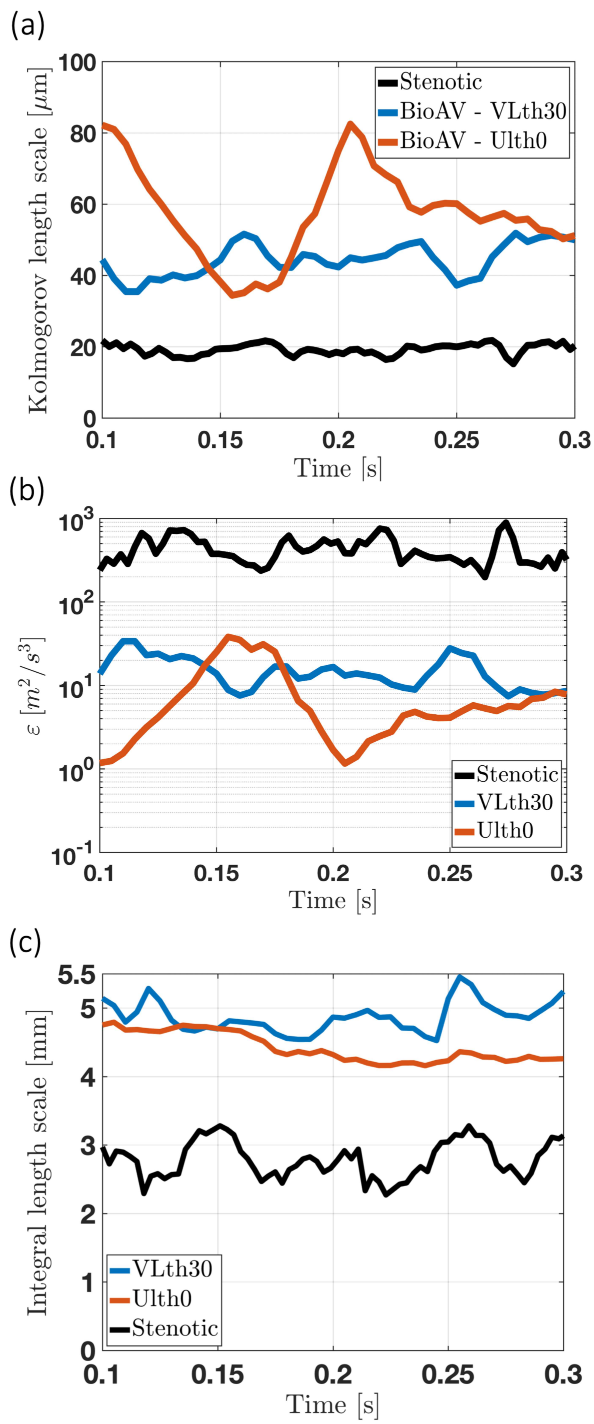

Figure 2: Time series of turbulence characteristics for the three valvular cases over the systolic phase. (a) Kolmogorov length scale. (b) Dissipation rate of turbulent kinetic energy ε. (c) Integral length scale $\mathfrak{L}$.

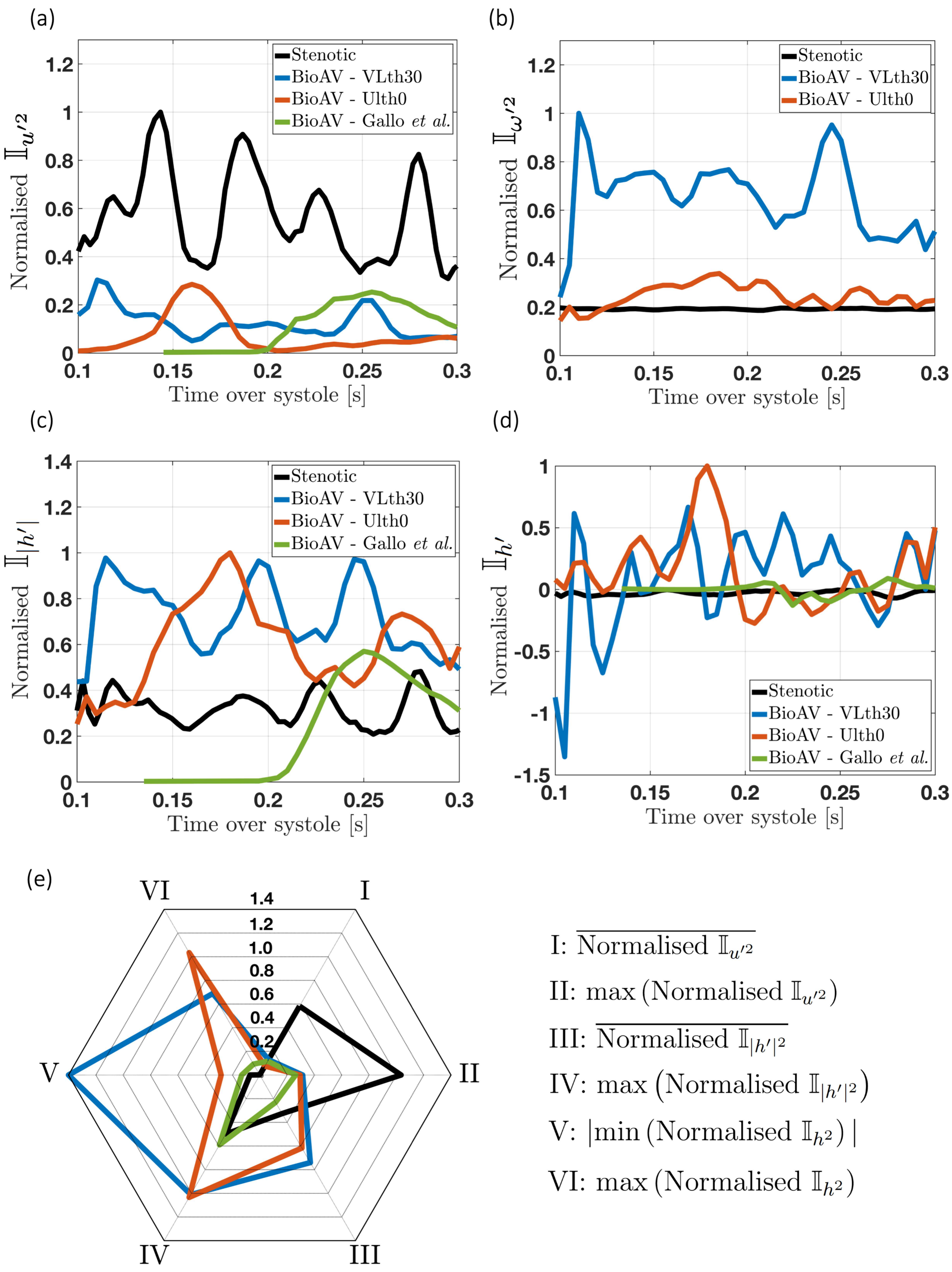

Figure 3: Time series over systole of normalised (a) intensity of fluctuating KE, (b) intensity of fluctuating enstrophy, (c) intensity of unsigned fluctuating helicity and (d) intensity of signed fluctuating helicity. The three valvular cases investigated in this study are plotted along with the valvular case presented in Gallo *et al.*[13]. (e) Spider chart of the time-averaged ($\overline{\circ}$) and maximum normalised $\mathbb{I}_{u'^2}$ (I and II) and $\mathbb{I}_{|h'|^2}$ (III and IV). The maximum and absolute minimum values of normalised $\mathbb{I}_{h'^2}$ is also displayed (V and VI).

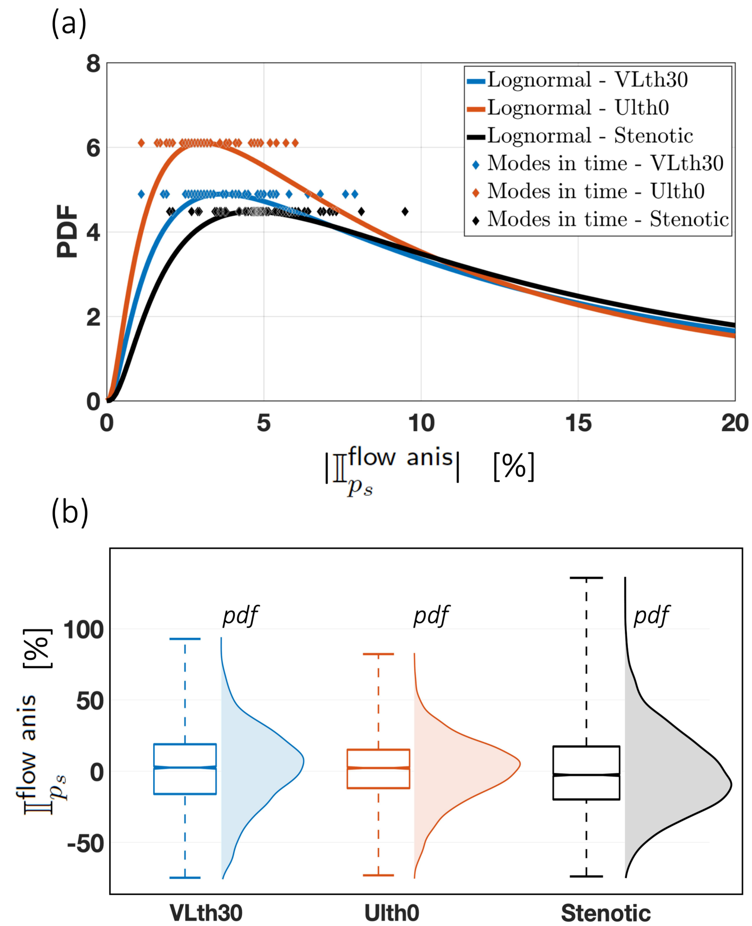

Figure 4: Probability distributions of the modal KE anisotropy intensity. (a) Fitted log-normal probability density function (PDF) for the three valve configurations, the mode of the PDFs was used in the spectral analysis part of the study. The rhombi represent the modes of the log-normal distribution fitted for each instant considered over peak systole. (b) Boxplots and distribution for the comparison of the shape of the distributions for the three valvular cases.

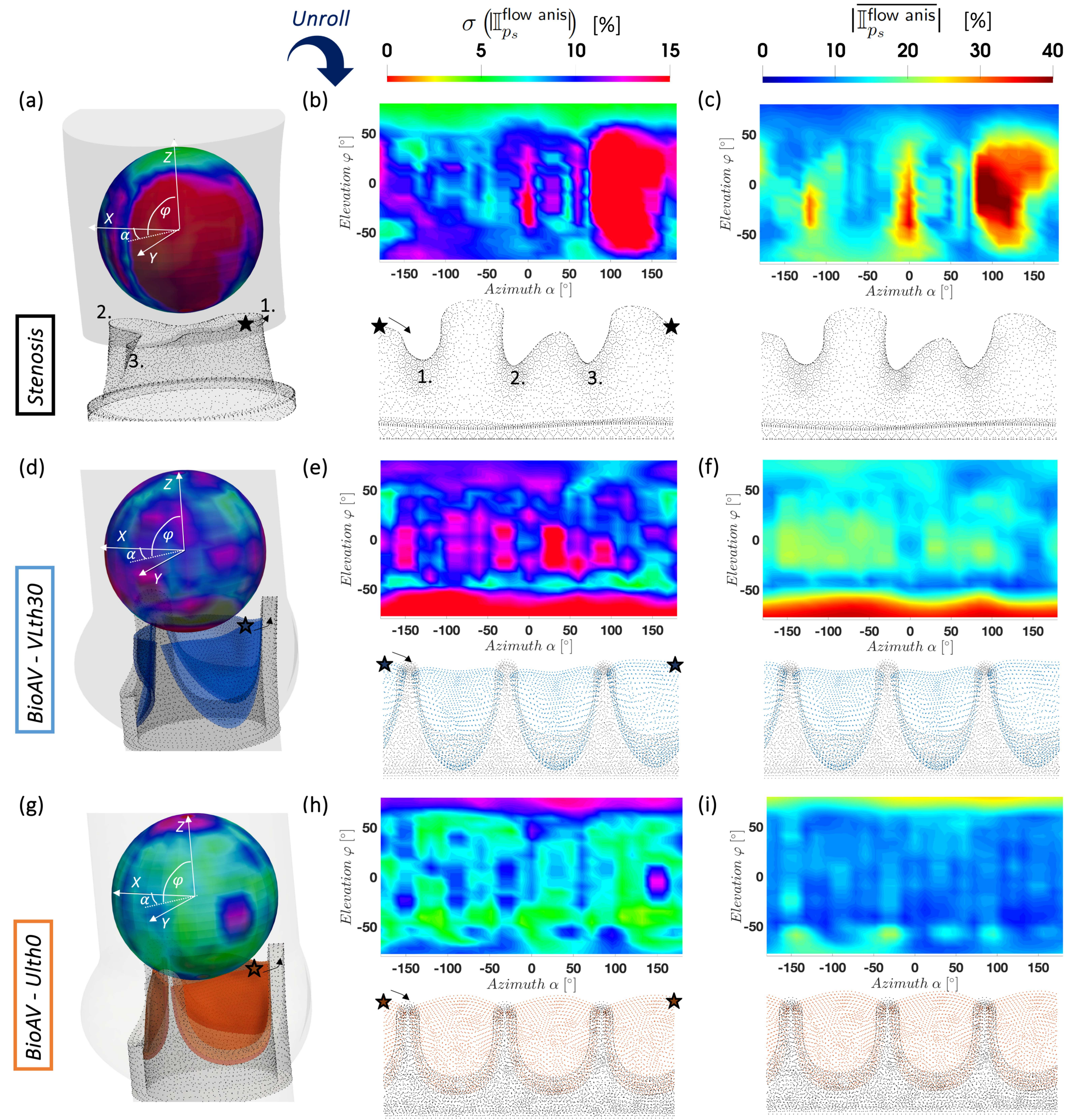

Figure 5: Spatial distribution and statistical description, including the standard deviation σ and the temporal average value of the time-dependent modal KE anisotropy fields $|\overline{\mathbb{I}_{p_s}^{\text{flow anis}}}|$ obtained on spherical shells near the valvular orifice. The geometries of the spheres and orifice are projected onto a rectangular map using a cylindrical map projection, also known as the Mercator projection. In this map, the azimuthal angle α is represented on the x-axis and the elevation angle φ is represented on the y-axis. The stenotic case is presented in (a, b, c), the valvular case with the design VLth30 in (d, e, f) and the case of the BioAV with the design Ulth0 in (g, h, i).

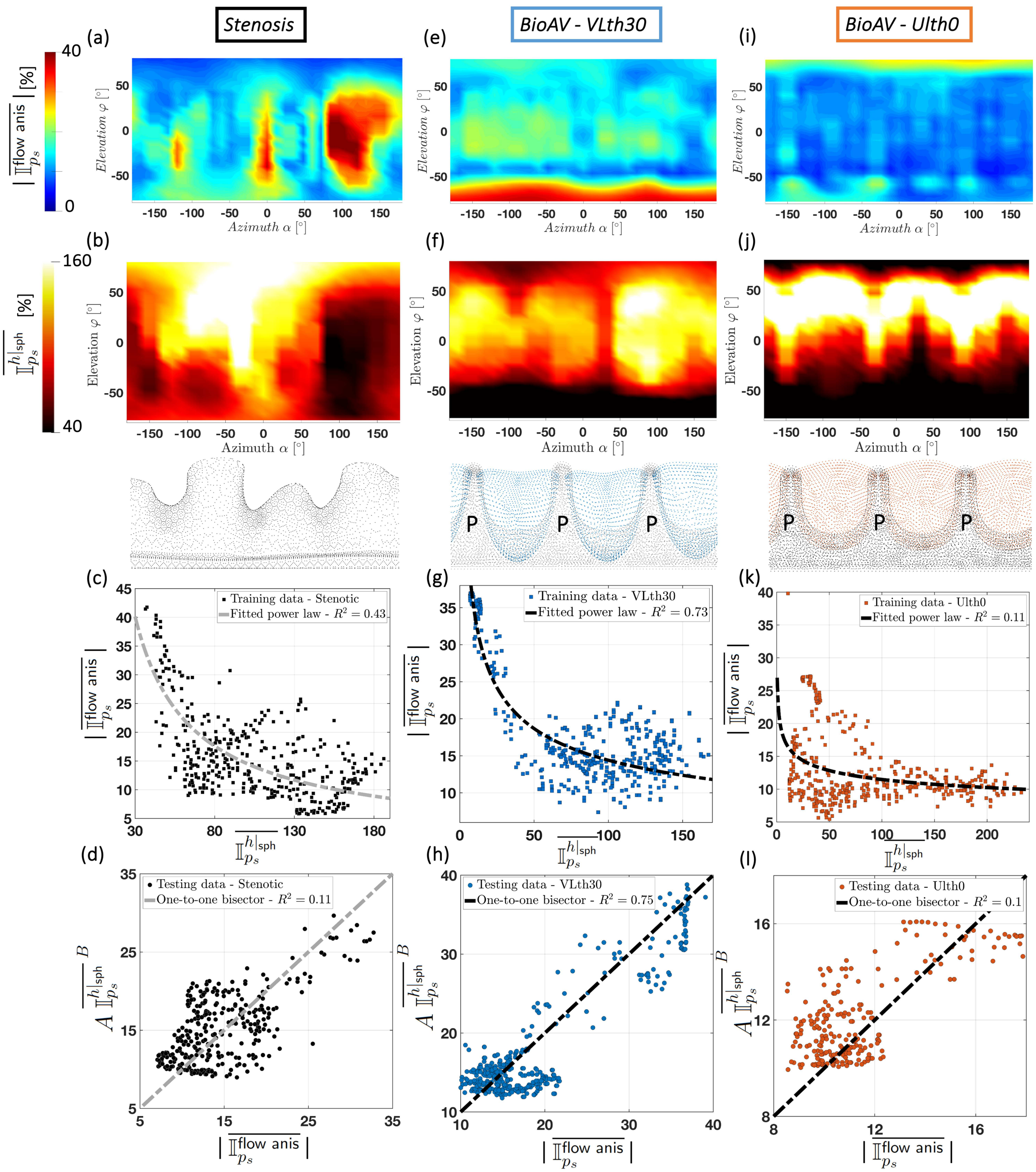

Figure 6: Anti-correlation between $\overline{|\mathbb{I}^{\text{flow anis}}_{p_s}|}$ and $\overline{\mathbb{I}^{h|_{\text{sph}}}_{p_s}}$ over spherical shells close to the valvular orifice (cf. Fig. 8). The colour-coded distribution map of the temporal average of $|\mathbb{I}^{\text{flow anis}}_{p_s}|$ for the three valvular configurations under consideration is displayed in (a, e, i). The distribution heat map of time-averaged normalised helicity intensity $\mathbb{I}^{h|_{\text{sph}}}_{p_s}$ is displayed in (b, f, j) for the three valvular cases. (c, g, k) Scatter plots of $\overline{|\mathbb{I}^{\text{flow anis}}_{p_s}|}$ as a function of $\overline{\mathbb{I}^{h|_{\text{sph}}}_{p_s}}$. The two coefficients A and B of a power law correlating the two quantities are fitted through the resolution of a non-linear least-square minimisation problem[7,8,27]. The accuracy of the training prediction is evaluated using the coefficient of determination R^2. The accuracy of the prediction based on the testing dataset points for the three valvular cases is presented in (d, h, l).

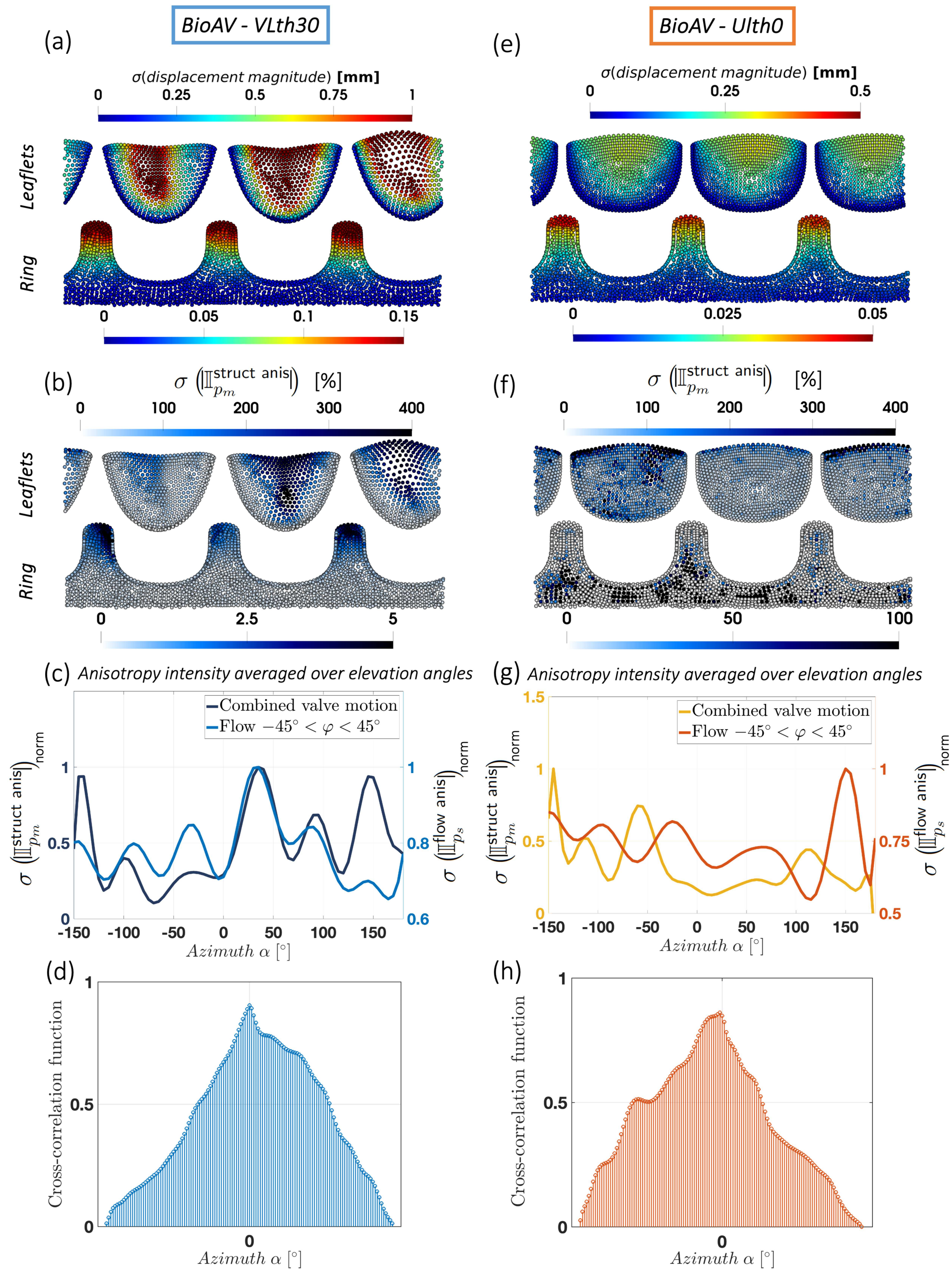

Figure 7: Comparison and correlation between the anisotropy in the leaflet and ring motion of the two bioprosthetic valves (VLth30 and Ulth0) and anisotropy of the modal kinetic energy in the flow in the vicinity of the valve orifice. (a, e) Standard deviation σ of the unrolled point distribution of the anisotropy intensity based upon the valve kinetic energy. (b, f) Standard deviation σ of the time-dependent unrolled spatial distribution of the displacement magnitude in the two valves. (c, g) Comparison of the standard deviation of the anisotropy intensity in the valve motion and in the flow averaged over the elevation angle φ as a function of the angle α. (g, h) Cross-correlation functions between the two $\sigma\left(\mathbb{I}_{p_s}^{\text{flow anis}}\right)_{\text{norm}}$ and $\sigma\left(\mathbb{I}_{p_m}^{\text{struct anis}}\right)_{\text{norm}}$ curves as a function of α.

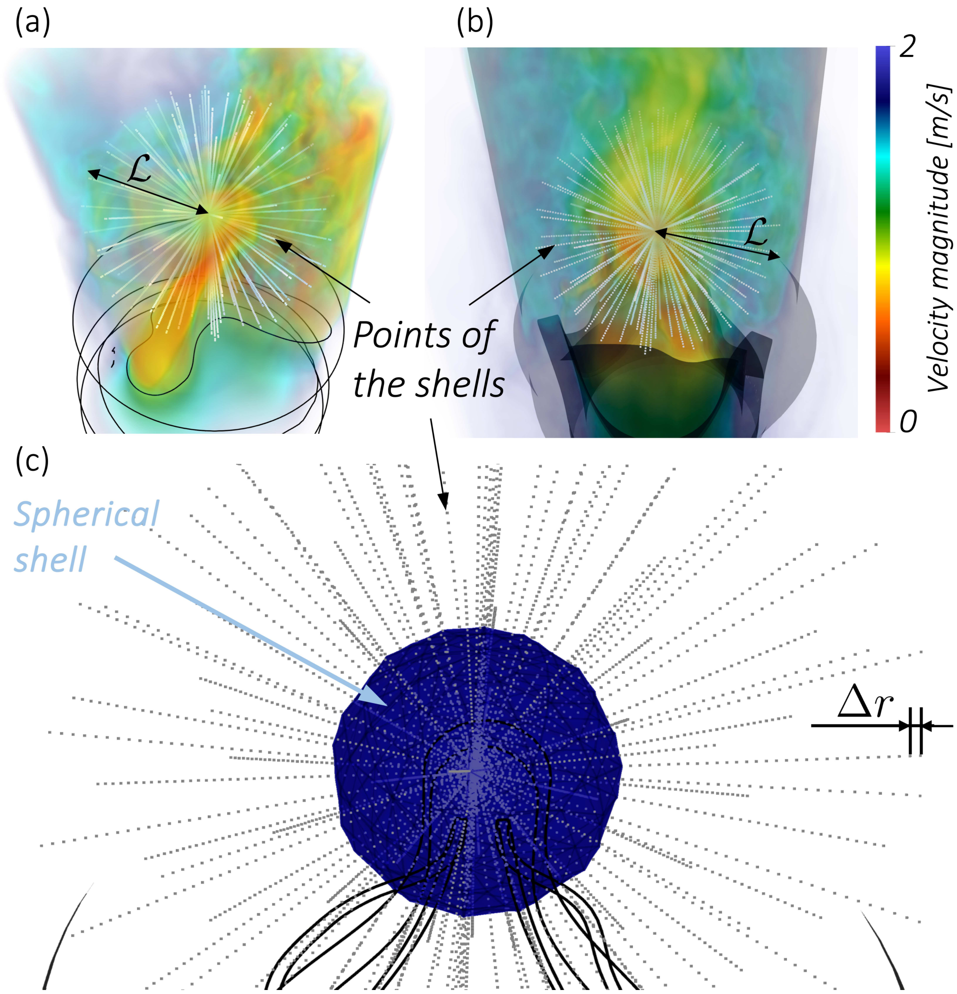

Figure 8: Definition of the points on spherical shells for the computation of the Fourier modes and of the first-order autocorrelation function as part of the spectral analysis for (a) the stenotic case and (b) one of the BioAV cases (VLth30). The spherical surface consists of 122 points as displayed in (c) equally spaced by a distance Δr of 125 m in the stenotic case and 250 m in the BioAV cases. The largest radius $\mathcal{L}$ for the spherical shell is equal to 10 mm and 11.5 mm for the stenotic and BioAV cases, respectively. The centre of the spheres is on the centreline of the straight ascending aorta. The instantaneous velocity magnitude is visualised in (a) and (b) through volumetric rendering displaying the jet of high velocity issuing from the valvular orifice.

Supplementary Files

This is a list of supplementary files associated with this preprint. Click to download.

- ManuscriptvalveDesignPart2PasSINatBiomed.pdf